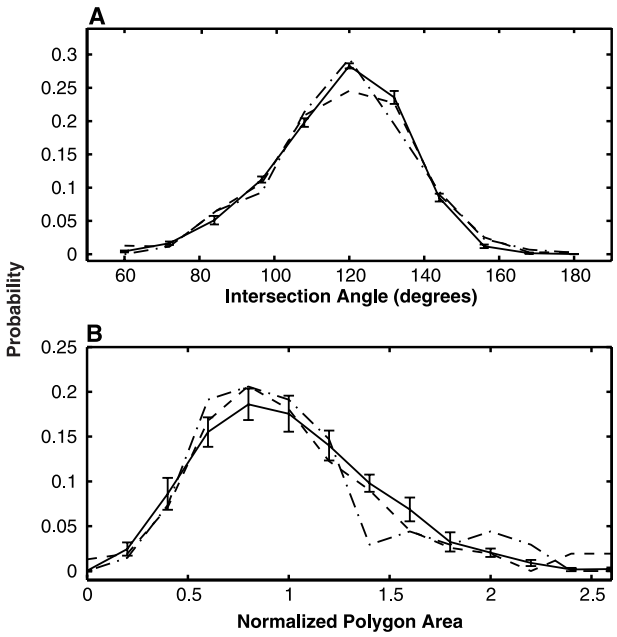

Fig. 5. (**A**) Intersection angle and (**B**) polygon area (normalized by the mean polygon area) probability distributions from sorted polygons in Alaska and predictions from the model using parameters as in Fig. 4, except with simulation size of 30 × 30 m. Dashed line, west pond; dash-dot line, east pond; solid line, model. Error bars represent SD of 10 independent model runs. Model is consistent with measurements within their level of variability.

References and Notes

1. A. L. Washburn, *Geol. Soc. Am. Bull.* **67**, 823 (1956).
2. A. E. Corte, *Biul. Peryglacjalny* **15**, 175 (1966).
3. S. P. Anderson, *Geol. Soc. Am. Bull.* **100**, 609 (1988).
4. S. Taber, *J. Geol.* **37**, 428 (1929).
5. A. C. Fowler, W. B. Krantz, *SIAM J. Appl. Math.* **54**, 1650 (1994).
6. N. Li *et al.*, *Cold Regions Sci. Technol.* **31**, 199 (2000).
7. N. Matsuoka, *Earth Sci. Rev.* **55**, 107 (2001).
8. R. J. Ray *et al.*, *J. Glaciol.* **29**, 317 (1983).
9. K. J. Gleason *et al.*, *Science* **232**, 216 (1986).
10. B. T. Werner, B. Hallet, *Nature* **361**, 142 (1993).
11. M. A. Kessler *et al.*, *J. Geophys. Res.* **106**, 13287 (2001).
12. B. Hallet, *Can. J. Phys.* **68**, 842 (1990).
13. B. T. Werner, T. M. Fink, *Science* **260**, 968 (1993).
14. A. B. Murray, C. Paola, *Nature* **371**, 54 (1994).
15. B. T. Werner, *Geology* **23**, 1107 (1995).
16. H. H. Stolum, *Science* **271**, 1710 (1996).
17. P. Rohani *et al.*, *Trends Ecol. Evol.* **12**, 70 (1997).
18. G. Nicolis, I. Prigogine, *Self-Organization in Nonequilibrium Systems: From Dissipative Structures to Order Through Fluctuations* (Wiley, New York, 1977).
19. J. H. Schmertmann, R. S. Taylor, *Quantitative Data from a Patterned Ground Site over Permafrost* (U.S. Army Cold Regions Research and Engineering Laboratory, Hanover, NH, 1965).
20. F. H. Nicholson, *Arctic Alpine Res.* **8**, 329 (1976).
21. F. A. Cook, *Arctic* **8**, 237 (1955).
22. The lateral sorting feedback is consistent with the limited range of relevant field observations. Frost-susceptible soils overlain by surface stone layers often exhibit lateral sorting associated with soil plugs rising to the surface (*34*). A model for sorted circles based on this lateral sorting feedback is quantitatively consistent with field measurements (*11*).
23. Observations within sorted polygons of upended stones, stones aligned parallel to the stone domain axis, and mud folds parallel to the stone-soil contact are consistent with lateral squeezing of stone domains (*35, 36*).
24. Surface relief across stone domains reflects removal of soil from beneath by frost heave at the stone-soil interface. Because stone domains narrow with depth, frost heave near the ground surface removes soil beneath the edge of the stone domain, whereas frost heave at depth removes soil beneath the center. In steady state, surface gradients are balanced by stone avalanching and removal of soil is balanced by soil addition processes whose impact on elevation is distributed across the stone domain surface.
25. Lateral squeezing is dependent on stone domain width (relative to stone diameter) owing to increased resistance to deformation by narrower stone domains.
26. See supporting data on *Science* Online.
27. Unlike previous simulation models (*10, 11, 37*), stone position is not discretized, avoiding congestion effects that can cause trapping and jamming of stones on lattices. However, here a lattice with grid size corresponding to stone diameter is used to calculate the concentration of stones and to determine the depth to which they are stacked. This semicontinuous algorithm allows for greater sensitivity to local biases because stones can move in any direction and over distances less then a cell width. Stones can also overlap, representing stacking of stones, up to a limit corresponding to the maximum depth of freeze-thaw processes.
28. The length scale D_{ls} corresponds to the maximum lateral distance over which soil is displaced by frost heave (*11*).
29. K_{ls} and K_{sq} are likened to diffusion constants because they quantify the ratio of stone flux to gradient.
30. The magnitude of squeezing depends on the thickness of the ice-rich layer along the near-vertical boundaries between stone and soil domains. Squeezing can be influenced by soil domain size for small soil domains, but well-formed soil domains generally are much larger than the thickness of the ice-rich layer. Therefore, this dependence is not included in the model (i.e., D_{sq} does not depend on soil domain size).
31. D. Weaire, N. Rivier, *Contemp. Phys.* **25**, 59 (1984).
32. F. Elias *et al.*, *Phys. Rev. E* **56**, 3310 (1997).
33. Measured sorted polygons were located in the basins of two desiccated ponds 100 m north of Denali Highway, ~115 km east of Cantwell, Alaska. Both ponds exhibit a gradation from high to low stone concentration moving outward from their centers. Well-formed polygons with narrow stone domains located midway in this gradation were digitized from low-elevation aerial photographs that had been orthorectified using ground control points (*38*). East pond: 68 polygons, 436 angles. West pond: 155 polygons, 705 angles.
34. A. L. Washburn, *Plugs and Plug Circles: A Basic Form of Patterned Ground, Cornwallis Island, Arctic Canada—Origin and Implications* (Geological Society of America, Boulder, CO, 1997).
35. R. P. Goldthwait, *Quat. Res.* **6**, 27 (1976).
36. J. S. Huxley, N. E. Odell, *Geogr. J.* **63**, 207 (1924).
37. F. Ahnert, *Trans. Jpn. Geomorphol. Union* **2**, 301 (1981).
38. Y. I. Abdel-Aziz, H. M. Karara, *Proceedings of the Symposium on Close-Range Photogrammetry* (American Society of Photogrammetry, Falls Church, VA, 1971), pp. 1–18.

39. We thank A. B. Murray and B. Hallet for many helpful discussions, and L. Clarke for assistance in image processing. Supported by NSF Arctic Natural Sciences Program grant OPP-9530860, the Andrew W. Mellon Foundation, a National Defense Science and Engineering Graduate Fellowship, and a student research grant from the Whole Earth Society at Scripps Institution of Oceanography.

Supporting Online Material

www.sciencemag.org/cgi/content/full/299/5605/380/DC1
SOM Text
Fig. S1

13 August 2002; accepted 19 November 2002

The Global Morphology of Wave Poynting Flux: Powering the Aurora

A. Keiling,[1]*† J. R. Wygant,[1] C. A. Cattell,[1] F. S. Mozer,[2] C. T. Russell[3]

Large-scale, electric currents flowing along magnetic field lines into the polar regions of Earth are thought to be the main contributors of the energy that powers the ionospheric aurora. However, we have found evidence for global contributions from electromagnetic waves (Alfvén waves). Data that were collected from the Polar spacecraft over the course of 1 year show that the flow of wave electromagnetic energy at altitudes of 25,000 to 38,000 kilometers delineates the statistical auroral oval. The Poynting flux of individual events distributed along the auroral oval was larger than 5 ergs per square centimeter per second, which is sufficient to power auroral acceleration processes. This evidence suggests that in addition to magnetic field-aligned currents, the dayside and nightside aurora is globally powered by the energy flow of these high-altitude Alfvén waves.

Earth's aurora occurs statistically and often simultaneously in an oval-shaped belt (Fig. 1A) around the magnetic poles (*1*). Magnetic field lines connect this auroral oval to the magnetosphere, the region above the atmosphere that is dominated by Earth's magnetic field and filled

with plasma. The dayside and nightside auroras are associated with different magnetospheric phenomena (*2*). The nightside aurora is the result of the sudden release (over the time period of tens of minutes to hours) of large amounts of energy, which is periodically extracted from the solar wind and stored in the magnetic field of the magnetotail (*3*). Through an unknown sequence of energy transfer processes, a large fraction of this energy is transported to the auroral acceleration region (located at an altitude of 5000 to 15,000 km above the polar regions) (*4*), where electron energization processes occur to create the intense electron beams that cause the aurora. In contrast, the dayside aurora is connected to the cusp region and is driven by uncertain mechanisms. In either case, it is expected that the aurora is powered by energy flow along the magnetic field lines. However, the altitude away from the ionosphere at which the energy flow becomes dominantly field-aligned has not been determined. In addition, the form of energy that dominates is not known, considering that it could be either kinetic particle energy or electromagnetic energy carried by quasi-static field-aligned currents (FACs) [for a tutorial on FACs in space, see (*5*)] or Alfvén waves (*6*). To understand the auroral phenomenon, we need to identify all contributing energy carriers. Here, we determined the global morphology of the Poynting flux due to electromagnetic waves, which are also called Alfvén waves (*6*), on auroral field lines at altitudes of 25,000 to 38,000 km above ground by using electric and magnetic field data (*7*, *8*) that were collected for one year by the Polar spacecraft (*9*).

In addition to in situ measurements, the Ultraviolet Imager (UVI) (*10*) onboard Polar takes images of ionospheric auroral emissions. These images show the global morphology of auroras in the UV spectrum, but they can also be used to estimate energy depositions through electron beams into the ionosphere causing the auroral emissions. The average global distribution of auroral luminosity in the Northern Hemisphere derived from a large set of images taken over a period of 4 months coincides with the statistical location of the auroral oval with three distinct emission intensifications centered at 22:30, 15:00, and 09:00 local time (Fig. 1B) (*11*).

During the period from 1 January 1997 to 31 December 1997, the Polar spacecraft completed about 470 orbits. The wave Poynting fluxes ($\mathbf{S} = \delta\mathbf{E} \times \delta\mathbf{B}/\mu_0$) were calculated for the entire database from the electric ($\delta\mathbf{E}$) and magnetic ($\delta\mathbf{B}$) wave perturbation fields in the period range from 6 to 180 s (*12*). This period range was chosen based on the results of previous Polar studies (*13*, *14*) that showed the existence of large Alfvén waves in this range in the plasma sheet during auroral and substorm activity. This filtering removes any Poynting flux caused by large-scale FACs (Fig. 2). It also excludes any wave activity below 5.5 mHz, as previously reported (*15*). To obtain the component of the wave Poynting flux that flows along the background magnetic field, the wave Poynting flux, **S**, was projected onto the background magnetic field, **B** ($S_{\parallel} = S \cdot \mathbf{B}/|\mathbf{B}|$). To reduce the effect of standing waves, which change their Poynting flux direction periodically (and, thus, do not contribute to a net energy transfer), we averaged the Poynting flux over 30-s intervals. All of the Poynting flux values were scaled along converging magnetic field lines to ionospheric altitudes (~100 km) under the assumption of dissipationless propagation for the sake of comparing in situ values with ionospheric values (*16*). The database was then binned (2° × 0.75 hours per bin) according to magnetic latitude and local time. For each bin, two values were calculated: the average of all positive Poynting flux values (downward-directed Poynting flux) and the average of all negative values (upward-directed Poynting flux). The distribution of the downward-directed Poynting flux (Fig. 1C) delineates the auroral oval. Two regions of enhanced intensity occur at about 21:00 to 00:00 and at about 15:00 local time. The general location and intensity distribution of this high-altitude wave Poynting flux is very similar to the global auroral luminosity (Fig. 1B). Both ovals are displaced equally far

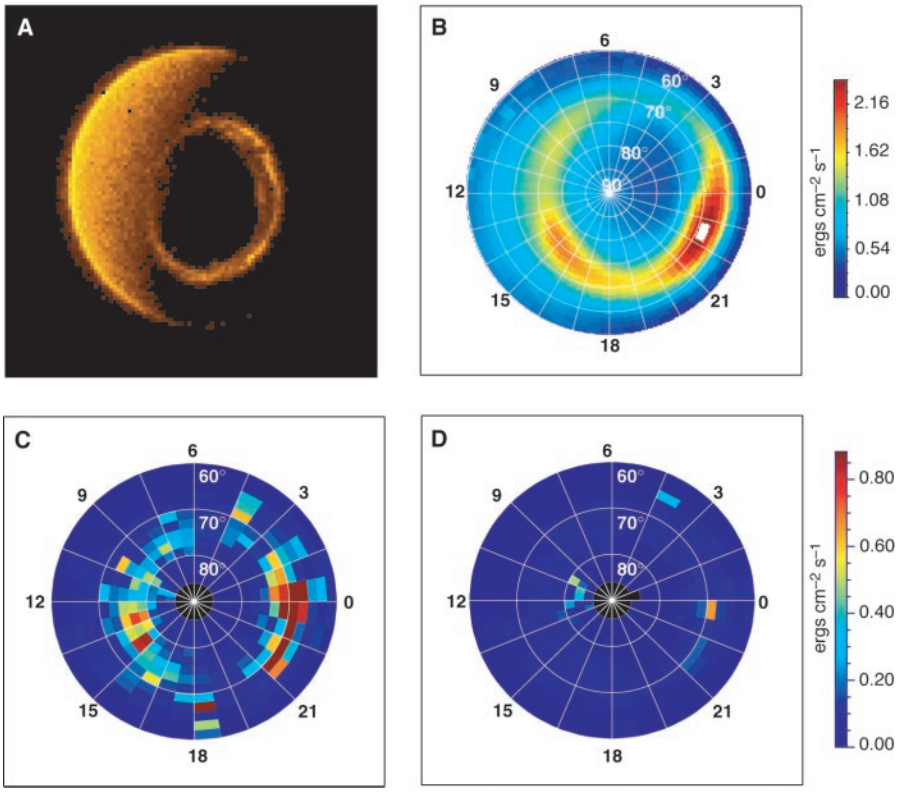

Fig. 1. Morphology of the aurora as seen from two cameras onboard the Polar satellite and as inferred from in situ, high-altitude Poynting flux measurements from Polar. (**A**) The aurora in the visible spectrum over the Northern Hemisphere [the image from the Visible Imaging System camera (*26*)]. This image shows the instant global morphology of auroral luminosity delineating an oval-shaped band. The dayside is to the left. Scattered sunlight during the day makes the aurora invisible to the human eye. (**B**) A map of average auroral intensity in the Northern Hemisphere recorded in the UV spectrum [Lyman-Birge-Hopfield (long)]. This map is composed of 17,372 images taken by the UVI (*10*) during four months of operation (1 April 1997 to 28 July 1997). This figure is slightly modified from Liou *et al*. (*11*). The numbers around the outside circle are the local times at the given locations. The numbers down the middle of the plot are magnetic latitudes. (**C**) Average wave Poynting flux flowing toward Earth as measured at high altitude (25,000 to 38,000 km) in the Northern Hemisphere obtained from 1 year of Polar measurements and then scaled along converging magnetic field lines to ionospheric altitudes (100 km). More intense downward Poynting flux (brown, red, and yellow) delineates the auroral oval. Blue indicates very little or no flux. (**D**) Similar to Fig. 1C but for upward Poynting flux (i.e., away from Earth). Very little return Poynting flux exists at high altitude.

[1]Department of Physics and Astronomy, University of Minnesota, Minneapolis, MN 55144, USA. [2]Space Science Laboratory, University of California, Berkeley, CA 94720, USA. [3]Institute of Geophysics and Planetary Physics, University of California, Los Angeles, CA 90024, USA.

*Present address: Centre d'Etude Spatiale des Rayonnements, Toulouse, France.

†To whom correspondence should be addressed. E-mail: akeiling@ham.space.umn.edu

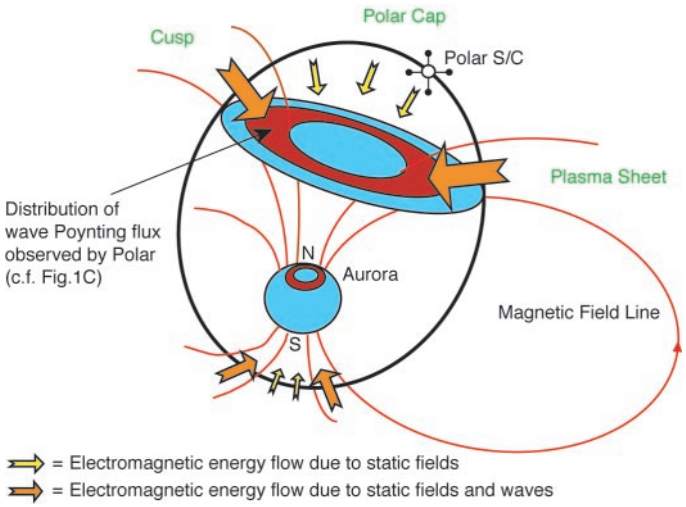

Fig. 2. Sketch of Polar's orbit and the two contributions of Poynting flux flowing along magnetic field lines into the polar region. Three distinct regions exist above the polar region and extend out into space: cusp, polar cap, and plasma sheet. The Polar spacecraft crosses these regions on an elliptical, polar orbit at altitudes between 25,000 and 38,000 km in the Northern Hemisphere. During the course of 1 year, the orbital plane precesses by 360°. The Poynting flux is carried by static fields (convection electric fields and magnetic fields associated with FACs) and Alfvén waves. It is mostly dissipated by Joule heating in the ionosphere and particle acceleration in the auroral acceleration region. The in situ wave Poynting flux measured by Polar delineates the statistical location of auroras.

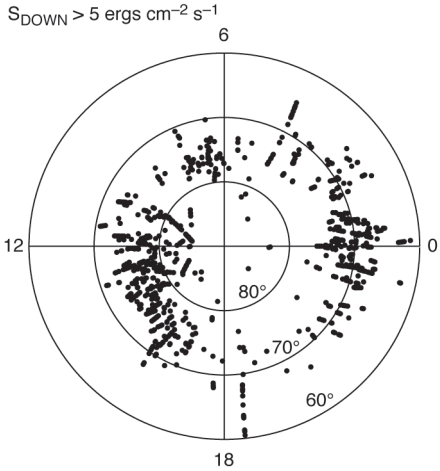

Fig. 3. Distribution of events with Poynting flux larger than 5 ergs cm^{-2} s^{-1} (mapped along converging magnetic field lines into the ionosphere, ~100 km) recorded by Polar versus latitude and local time. The events approximately delineate the statistical location of auroras. Two long traces of large Poynting flux events (at about 18:20 and about 04:30 local time) occurred on 10 January 1997 and 3 August 1997. During both orbits, geomagnetic storms prevailed. Geomagnetic storms are periods of enhanced energy transfer over an extended period of time (from one to many days) compared with 30 min to 3 hours for auroral substorms. Polar recorded enhanced Poynting flux throughout the plasma sheet on these days, which accounts for the long traces.

(several degrees) antisunward from the magnetic north pole, and the two brightest regions in Fig. 1B nearly coincide with the two brightest regions in Fig. 1C. This similarity suggests a correlation between the global energy flow at Polar's altitude and the auroral oval in the ionosphere. In contrast, very little wave Poynting flux is flowing away from the ionosphere (Fig. 1D), which implies that the downward-directed wave Poynting flux (Fig. 1C) is not reflected back from the ionosphere but must be dissipated below the spacecraft's altitude, presumably in the auroral acceleration region.

The wave Poynting flux at high altitude (Fig. 1C) can account for about 30 to 35% of the energy flux required to cause the global ionospheric auroral luminosity (Fig. 1B). This value is an estimate, because the time periods used to generate the two distributions are not the same and auroral activity varies throughout the year. Nevertheless, this result suggests that the wave Poynting flux is a substantial contributor of energy flux for auroral processes. Our data (Fig. 1, C and D) show the global morphology of wave Poynting flux averaged over many spacecraft passes, which include quiet (no aurora) and active (aurora) times. Similarly, the distribution derived from UV images (Fig. 1B) shows the average distribution. Therefore, the energy fluxes shown in all three figures do not show the instantaneous energy flux associated with an auroral display. To determine whether the energy flux for individual events observed by Polar is itself sufficient to power auroral emissions, we searched for all the events in the database that would have a Poynting flux larger than 5 ergs cm^{-2} s^{-1} when scaled to 100-km altitude (i.e., data points were not averaged over the bin size, as was done for Fig. 1, C and D). We chose 5 ergs cm^{-2} s^{-1} as the threshold because the weakest electron beams that can produce visible auroral emissions have energy fluxes of ~1 ergs cm^{-2} s^{-1} at ionospheric altitudes (*17*). Thus, each such event would carry a sufficient Poynting flux to create auroral emissions. We found that all events are located approximately along the auroral oval and more events cluster in the postnoon and midnight sectors (Fig. 3), a pattern that is similar to Fig. 1C. This result shows that individual events distributed along the entire auroral oval carry sufficient energy flux to power ionospheric auroral emissions. In addition, many events had larger values (>30 ergs cm^{-2} s^{-1}) of Poynting flux that can account for intense auroras as well.

Large-scale FACs have been considered the main carrier of the electromagnetic energy that powers auroral acceleration processes. Our observations modify the view that FACs are the only energy carrier globally providing electromagnetic energy to the auroral region. We found that Alfvén waves, which occur globally, play an important role in the creation of the aurora. Previous studies have reported wave Poynting flux in association with auroral phenomena in isolated events in different space regions: the inner edge of the plasma sheet (*18*), the cusp (*19*), the central plasma sheet (*20*, *21*), and the plasma sheet boundary layer (*13*, *14*). It has also been shown for about 20 to 25 events that the observed high-altitude wave Poynting flux was sufficient to power the magnetically conjugate auroral emissions (*13*, *22*). Our statistical study indicates that these case studies are not isolated occurrences. Most important, we found that the global distribution of auroral luminosity is closely related to the global distribution of high-altitude Alfvén waves. This correlation shows that the ionosphere and the magnetosphere are electrodynamically coupled via Alfvén waves over the entire auroral region. Furthermore, the magnitude and the flow direction of the wave Poynting flux that is carried by the Alfvén waves suggest that this wave Poynting flux is a major energy contributor for auroral acceleration processes and, ultimately, for auroral emissions along the entire auroral oval. The globally occurring Alfvén waves thus provide an important link in the chain of energy transfer processes from the magnetosphereto the aurora. To increase our understanding of energy transfer processes in the magnetosphere, the next step is to compare the wave Poynting flux distribution reported here with corresponding global distributions of particle energy flux and Poynting flux associated with large-scale FACs at the same altitude. Such a comparison has only been made for one large-amplitude Poynting flux event. It was shown (*23*) that the enhanced wave Poynting flux coincided with a slightly smaller enhancement in the particle energy flux and that it was one to two orders of magnitude larger than the electromagnetic energy flux associated with local FACs.

References and Notes

1. S.-I. Akasofu, *Planet. Space. Sci.* **14**, 587 (1966).
2. C.-I. Meng, R. Lundin, *J. Geophys. Res.* **91**, 1572 (1986).

3. D. N. Baker *et al.*, *J. Geophys. Res.* **102**, 7159 (1997).
4. P. H. Reiff *et al.*, *Geophys. Monogr. Ser.* **80**, 143 (1993).
5. S. W. H. Cowley, *Geophys. Monogr. Ser.* **118**, 91 (2000).
6. Alfvén waves, first predicted by Hannes Alfvén (*24*), are electromagnetic-hydromagnetic waves that require a plasma for propagation. Guided along magnetic field lines, Alfvén waves carry energy from one space region to another. The generation mechanisms of these waves in the magnetosphere are still under investigation.
7. P. Harvey *et al.*, in *The Global Geospace Mission* (Kluwer Academic Press, Norwell, MA, 1995), pp. 583–596.
8. C. T. Russell *et al.*, in *The Global Geospace Mission* (Kluwer Academic Press, Norwell, MA, 1995), pp. 563–582.
9. The Polar spacecraft has an 18-hour polar orbit with perigee and apogee of ~7600-km and ~51,000-km altitude, respectively. During the course of one year, its orbital plane precesses by 360°, thus covering the entire Northern Hemisphere (Fig. 2).
10. M. R. Torr *et al.*, in *The Global Geospace Mission* (Kluwer Academic Press, Norwell, MA, 1995), pp. 459–495.
11. K. Liou *et al.*, *J. Geophys. Res.* **102**, 27197 (1997).
12. The perturbation fields were calculated from the full three-dimensional magnetic field vector and two components of the electric field. The reason for not using the azimuthal (spin-axis) electric field component, E_θ, is that this component is measured with a much shorter boom on the satellite and requires visual inspection in order to guarantee its accuracy. The large-database study presented here prohibits visual inspection. Fortunately, it was shown (*20*) that substorm-related electric fields at altitudes similar to those considered in our study are predominately polarized in the plane perpendicular to E_θ and, thus, the wave Poynting flux is largely due to the other two electric field components, which lie in the orbital plane, and the azimuthal magnetic field component. As a check, we have performed the data analysis when E_θ is set to zero and when E_θ is unchanged. The qualitative conclusions are identical. We present here the results for $E_\theta = 0$.
13. J. R. Wygant *et al.*, *J. Geophys. Res.* **105**, 18675 (2000).
14. A. Keiling *et al.*, *Geophys. Res. Lett.* **27**, 3169 (2000).
15. J. Samson *et al.*, *J. Geophys. Res.* **96**, 15683 (1991).
16. The effect of converging field lines is to amplify the Poynting flux as it approaches Earth in proportion to the magnetic field strength, *B*. The Poynting flux, *S*, at different altitudes scales as $S_I = S_H \times B_I/B_H$, where the indices indicate the ionospheric (I) and the high-altitude (H) values.
17. Electromagnetic energy is converted into kinetic particle energy by energization processes that are not fully understood yet (*25*) at altitudes between 5000 and ~15,000 km (*14*).
18. N. C. Maynard *et al.*, *J. Geophys. Res.* **101**, 7705 (1996).
19. C. C. Chaston *et al.*, *Geophys. Res. Lett.* **26**, 647 (1999).
20. A. Keiling *et al.*, *J. Geophys. Res.* **106**, 5779 (2001).
21. P. K. Toivanen *et al.*, *J. Geophys. Res.* **106**, 19117 (2001).
22. A. Keiling *et al.*, *J. Geophys. Res.* **107**, 10.1029/2001JA900140 (2002).
23. J. R. Wygant *et al.*, *J. Geophys. Res.* **107**, 10.1029/2001JA900113 (2002).
24. H. Alfvén, *Nature* **150,** 405 (1942).
25. R. L. Lysak, M. André, *Phys. Chem. Earth Ser. C* **26**, 3 (2001).
26. L. A. Frank *et al.*, in *The Global Geospace Mission* (Kluwer Academic Press, Norwell, MA, 1995), pp. 297–328.

27. We thank L. Frank and K. Liou for providing Fig. 1, A and B, respectively. NASA supported the analysis of the electric field data (grant NAG 5-3182) and the analysis of the magnetic field data (grant NAG 5-7721).

5 August 2002; accepted 3 December 2002

Ancient Tripartite Coevolution in the Attine Ant-Microbe Symbiosis

Cameron R. Currie,[1,2,3,4]* Bess Wong,[3] Alison E. Stuart,[1] Ted R. Schultz,[5] Stephen A. Rehner,[6] Ulrich G. Mueller,[4,2] Gi-Ho Sung,[7] Joseph W. Spatafora,[7] Neil A. Straus[3]

The symbiosis between fungus-growing ants and the fungi they cultivate for food has been shaped by 50 million years of coevolution. Phylogenetic analyses indicate that this long coevolutionary history includes a third symbiont lineage: specialized microfungal parasites of the ants' fungus gardens. At ancient levels, the phylogenies of the three symbionts are perfectly congruent, revealing that the ant-microbe symbiosis is the product of tripartite coevolution between the farming ants, their cultivars, and the garden parasites. At recent phylogenetic levels, coevolution has been punctuated by occasional host-switching by the parasite, thus intensifying continuous coadaptation between symbionts in a tripartite arms race.

Symbiosis shapes all levels of biological organization, from individual cells to communities and ecosystems (*1–4*). The attine ant-microbe symbiosis is a paradigmatic example of the generation of organic complexity through symbiotic association (*5–13*). Fungus-growing ants in the tribe Attini maintain an obligate mutualism with the fungi they grow for food. In return, the ants provide the fungus with substrate for growth, a means of dispersal to new locations, and protection from competitors and parasites (*14–16*). Attine fungus gardens are frequently infected by a group of potentially devastating fungal parasite species in the genus *Escovopsis* (*11–13*). A fourth symbiont in the attine symbiosis, a filamentous bacterium (actinomycete), is cultured by the ants on specialized body surfaces to derive antibiotics that inhibit the growth of *Escovopsis* (*10*, *12*, *17*). The ant-cultivar-parasite-bacterium association thus is a quadripartite symbiosis and one of the most complex symbiotic associations discovered in nature. Although the coevolution of attine ants and their fungal cultivars has been the subject of previous investigations (*5*, *6*, *8*, *18*), nothing is known about the evolution of the *Escovopsis* parasites or the attine bacterial mutualists. Here, we reconstruct the evolutionary history of *Escovopsis* to elucidate its origins and coevolution with fungus-growing ants and their domesticated fungi.

The attine ants, a monophyletic group of 13 genera that includes over 210 described species, have apparently cultivated fungi for over 50 million years (*7*). This mutualism is characterized by ancient evolutionary congruence in which specific groups of attine ants have specialized on specific groups of fungal cultivars. The vast majority of basal (lower) attines exclusively cultivate a group of closely related fungi in the family Lepiotaceae (*5*, *8*). The derived (higher) attines, including the leaf-cutting ants, cultivate fungi that belong to two clades of leucocoprineous (Lepiotaceae) fungi, which are probably derived from the fungi cultivated by the lower attines (*5*). One lineage within the lower attine genus *Apterostigma* has secondarily switched to fungi in the family Tricholomataceae, and ants in this *Apterostigma* clade thus cultivate fungi that are distantly related to the lepiotaceous cultivars typical for all other attine ants (*5*). In contrast to the ancient evolutionary congruence between ants and their cultivars, at more recent phylogenetic levels within ant-cultivar groups, cultivars may be transferred laterally between ant nests (*5*, *8*, *18*, *19*), and on multiple occasions free-living leucocoprineous fungi have been domesticated by lower attine ants as novel cultivars (*5*, *8*, *18*).

The fungus gardens of attine ants are parasitized by microfungi in the genus *Escovopsis*. *Escovopsis* infections cause substantial reductions in garden biomass and indirectly reduce

[1]Department of Ecology and Evolutionary Biology, University of Kansas, Lawrence, KS 66045, USA. [2]Smithsonian Tropical Research Institute, Apartado 2072, Balboa, Republic of Panama. [3]Department of Botany, University of Toronto, Toronto, Ontario M5S 3B2, Canada. [4]Integrative Biology, University of Texas at Austin, Austin, TX 78712, USA. [5]National Museum of Natural History, MRC 188, Smithsonian Institution, Washington, DC 20013–7012, USA. [6]Insect Biocontrol Laboratory, U.S. Department of Agriculture, Agricultural Research Service, Building 011A, BARC-W, Beltsville, MD 20705, USA. [7]Department of Botany and Plant Pathology, Oregon State University, Corvallis, OR 97331, USA.

*To whom correspondence should be addressed. E-mail: ccurrie@ku.edu